Optimizing Interface Conductivity in Electronics

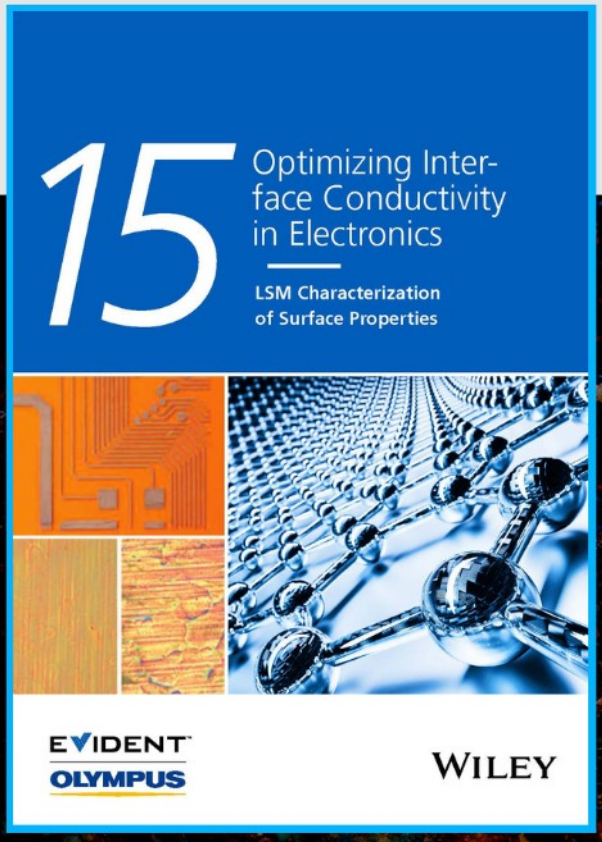

The latest eBook from Advanced Optical Metrology. Download for free.

Surface roughness is a key parameter for judging the performance of a given material's surface quality for its electronic application. A powerful tool to measure surface roughness is 3D laser scanning confocal microscopy (LSM), which will allow you to assess roughness and compare production and finishing methods, and improve these methods based on mathematical models.

Focus on creating high-conductivity electronic devices with minimal power loss using laser scanning microscopy is an effective tool to discern a variety of roughness parameters.

EVIDENT
OLYMPUS

WILEY

ADVANCED ELECTRONIC MATERIALS Open Access
www.advelectronicmat.de

Effect of Gadolinium on Electrical Properties of Polyethyleneimine Functionalized and Nitrogen-Doped Graphene Quantum Dot Nanocomposite Based Diode

Elif Orhan, Aslıhan Anter, Murat Ulusoy, Barış Polat, Can Okuyucu, Mustafa Yıldız, and Şemsettin Altındal*

Carbon, especially graphene quantum dots (GQDs) based electronics have become an attractive technology in recent years. The controlled modification of the electrical and optoelectronic properties of GQDs by physical/chemical processes or synthetic methods may lead to new applications. Gadolinium-doped polyethyleneimine (PEI) functionalized and nitrogen-doped graphene quantum dots (GdNPs-PEI@N-GQDs) are synthesized by a hydrothermal method to determine how doping carbon-based materials with Gd alters the electrical properties of the structure. The electrical properties of the GdNPs/PEI@N-GQDs nanocomposite-based diode are investigated using the current–voltage (*I–V*) technique and the capacitance and conductance voltage (*C–V* & *G/ω–V*) technique at 300 K in the frequency range of 0.5 to 500 kHz at ± 5 V. The rectification ratio (RR) is found to be 14 at a voltage of ±5 V. The rectifying behavior of the diode changes to an ohmic behavior after doping with Gd, compared to the Gd-free PEI@N-GQDs sample (2.8×10^4 at ±5 V). The results are expected to have an impact on the understanding of carbon-based electronics technology.

1. Introduction

Carbon-based electronics have become an attractive technology in recent years. It can be the potential to replace or complement optoelectronic devices based on metals and inorganic semiconductors. Because of their tunable bandgap, high absorption, and high carrier mobility, carbon allotropes such as carbon nanotubes (CNTs), graphene, fullerenes, and GQDs are of particular interest in photodetection.[1–3] GQDs, one of the carbon allotropes, are quasi-zero-dimensional carbon-based materials with excellent physical properties such as remarkable photostability,[4] high fluorescence quantum yield,[5,6] low cytotoxicity,[7] good biocompatibility,[8,9] and excellent water solubility.[10] These properties make them attractive candidates for optoelectronic applications and biological imaging,[11,12] solar cells,[13] light-emitting devices (LEDs),[14] and deep ultraviolet (UV) photodetection.[15] Doped carbon-based materials with rare earth metals are one of the most promising areas of nanotechnology. Especially carbon-based materials containing Gd have been particularly interesting due to their excellent properties in fluorescence/ magnetic resonance imaging (MRI). It has been demonstrated that they can also be used as contrast agents to improve information from MRI.[16,17] Gd, which is a silvery white metal, reacts slowly with moisture or atmospheric oxygen to form a black coating.[18,19] Gadolinium and its complexes are easily visualized in MRI because of its strong paramagnetism

E. Orhan, A. Anter, M. Ulusoy, Ş. Altındal
Department of Physics
Gazi University
Ankara 06500, Turkey
E-mail: eliforhan@gazi.edu.tr

B. Polat
Deparment of Industrial Engineering
Ankara Medipol University
Ankara 06050, Turkey

C. Okuyucu
Department of Metallurgical and Materials Engineering
Middle East Technical University
Ankara 06800, Turkey

M. Yıldız
Department of Chemistry
Çanakkale Onsekiz Mart University
Çanakkale 17100, Turkey

The ORCID identification number(s) for the author(s) of this article can be found under https://doi.org/10.1002/aelm.202300261

DOI: 10.1002/aelm.202300261

due to the seven unpaired electrons in its 4f shell. The combination of carbon-based nanomaterials with metallic or nonmetallic oxides and hydroxides can lead to new properties. The metallic form Gd and its compounds absorb neutrons and are used as shields in neutron radiography and nuclear reactors. In a literature study,[20] Gd^{3+} /Mn^{2+} doped nitrogen-containing graphene quantum dots (NGQDs) have been developed to provide GQDs with MRI capabilities and also as biocompatible contrast agents. In addition, the significantly neutron capture cross-section of gadolinium (49 000 barns;1 barn = 10^{-28} m^2)[21] is an advantage for the potential application of this design for neutron detection.[22] In one study,[23] Gd doped GaN Schottky diode for neutron detection was fabricated. It was characterized by *I–V*, *C–V*, and charge collection efficiency (CCE) measurements. According to their results, the device showed ohmic behavior. Gold, platinum, and niobium-doped devices reported in the literature[24–26] showed similar effects due to the presence of the midgap defect. This shows that the diode has changed from a typical rectifier to ohmic behavior after doping with these materials. The Gd-doped CQDs synthesized by Molaei[27] are promising candidates for use as multifunctional imaging probes and as MRI contrast agents in brain mapping applications and biomedical diagnosis. Single-atom Gd attached to graphene quantum dots is a highly potent and contrasting agent for obtaining high-resolution MRI and will offer opportunities for future sensitive clinical theranostics.[28] The synthesis, properties, and biomedical applications of Gd-based oxide and oxysulfate particles were examined.[29] The structural characterization and photoluminescence properties of $(Gd_{1-x}Er_x)_2O_3$ nano phosphorus, synthesized by the coprecipitation of layered precursors, have been studied.[30] Furthermore, charge transfer and the electronic structure of gadolinium oxide nanoparticles were investigated both experimentally and theoretically.[31] It has been observed that Gd-doped materials are sensitive to radiation and is to be suitable for applications in dosimeters for proton beams, X-ray beams, and electron beams.[32–34] In this context, the first step was to determine the diode parameters of the Gd-doped structure. It should be investigated whether it can be used as a radiation sensor in future studies.

In our previous studies,[35,36] we investigated the *I–V* and $C/(G/\omega)$–*V* properties of PEI functionalized and N-doped GQDs without Gd at frequency range 1 kHz to 2 MHz in the voltage range of −3 to +7 V. The Gd-free PEI@N-GQDs sample showed the negative capacitance (NC) behavior at low frequencies. In this work, both the effect of gadolinium on the electrical properties of GdNPs/PEI@N-GQDs-based diode and surface states/trap levels characterizations were presented by the *I–V* and $C/(G/\omega)$–*V* technique at 300 K in the frequency range of 0.5 to 500 kHz at ± 5 V.

2. Experimental Section

2.1. Synthesis of PEI Functionalized N-Doped GQDs and GdNPs/PEI@N-GQDs Nanocomposites

The citric acid (CA), $Gd(NO_3)_3{\cdot}6H_2O$, and PEI (Mw: 1300, 50 wt% in H_2O) were provided by Sigma–Aldrich. Hydrothermal synthesis of PEI@N-GQDs successfully achieved.[31,35,36] Details of how to synthesize PEI@N-GQDs are reported in our previous work.[35,36] The CA (3.60 g, 18.75 mmol) and PEI (2.34 g, 1.80 mmol) were dissolved in 50 mL of deionized distilled water. The solution was incubated in an autoclave at 250 °C for 5 h. The suspensions were centrifuged at 12 000 rpm for 10 minutes, and the supernatant was collected after cooling to room temperature. The PEI@N-GQDs nanoparticles were washed two times with deionized distilled water and one time with ethanol. To obtain Gd nanoparticles, the PEI@N-GQDs nanoparticles were then stored in a desiccator. For the synthesis of Gd nanoparticles and their nanocomposites, a solution of PEI@N-GQDs (1 g) in 100 mL of water was added to a 250 mL round bottom flask. Subsequently, 20 mL of 0.1 M $Gd(NO_3)_3$ solution was added to the mixture of PEI@N-GQDs. The mixtures were heated at 90 °C for 2 h to complete the reduction of the Gd(III) cation to Gd(0) nanoparticles (GdNPs), resulting in the formation of nanocomposites consisting of Gd nanoparticles and GdNPs/PEI@N-GQDs. The GdNPs/PEI@N-GQDs nanocomposite solutions were then cooled at room temperature. The suspension products were centrifuged at 12 000 rpm for 10 min, and the supernatant was collected. The GdNPs/PEI@N-GQDs nanocomposites were washed one time with deionized distilled water and ethanol. Nanocomposites were desiccated and stored for further use.

2.2. Fabrication of GdNPs/ PEI@N-GQDs Nanocomposite-Based Diode

p-type Si (100) wafers were used to fabricate the diode. Following cleaning procedures,[37,38] aluminum (Al-248 nm) ohmic contact a was first deposited on the unpolished surface of the p-Si wafer by physical vapor deposition (PVD). The resulting GdNPs/PEI@N-GQDs nanocomposites were then deposited on the polished surface of the p-Si wafer using a spin-coating technique. The spinning speed is 3000 rpm, and the spinning time was locked for 30 s. The film thickness is ≈25 nm. Finally, the Al circular contacts with a thickness of 128 nm were formed on the GdNPs/PEI@N-GQDs-p-Si by thermal evaporation using a circular metal mask with a diameter of 1 mm. Details of the synthesis of N-doped GQDs functionalized with PEI are included in our previous works.[35,36] The structure of the diode is shown in schematic form in **Figure 1**.

3. Results and Discussion

3.1. Characterization of the Prepared PEI@N-GQDs and GdNPs/PEI@N-GQDs Nanocomposites (FTIR, UV–Vis, HRTEM, XPS, and EDX)

Firstly, Fourier transform infrared spectroscopy (FTIR) analysis was carried out. **Figure 2**a shows FTIR spectra of the starting compounds Gd (III) nitrate the PEI@N-GQDs, and GdNPs/PEI@N-GQDs nanocomposites. In comparison with the spectrum of the starting PEI/N/GQDs,[35] the FTIR spectrum of the GdNPs/ PEI@N-GQDs nanocomposite shows characteristic changes in the frequencies of the functional groups. The OH, COOH, NH_2, NH, Ar-H, C-H, COO+C=N+C-N, C=C, and C-O vibrational bands are observed in the starting material PEI@N-GQDs[35] at 3553–3498–3446, 3367, 3320–3200, 3125, 3054,

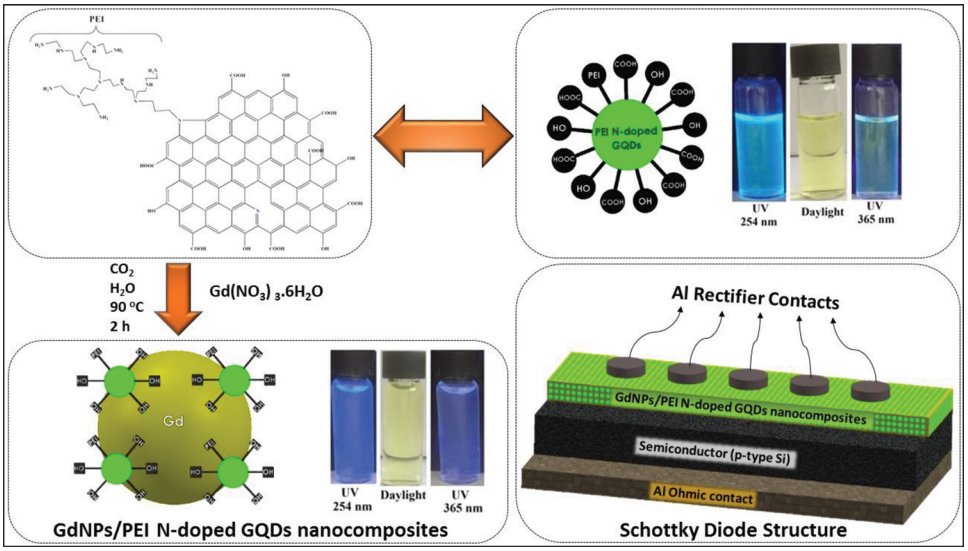

Figure 1. A schematic diagram of the GdNPs/PEI@N-GQDs nanocomposite-based diode.

2967–2839, 1646, 1559–1454, and 1305 cm^{-1}, respectively.[35] In the case of GdNPs/ PEI@N-GQDs nanocomposite, these vibration bands are observed at 3583 – 3495 – 3454 – 34 240, 3362–3305–3289, 3116, 3019, 2949, 1633, 1559, and 1311 cm^{-1}, respectively (Figure 2a).[35] COO, C=N, and C-N absorptions overlapped in the FTIR spectra of both PEI@N-GQDs and GdNPs/ PEI@N-GQDs nanocomposites.[35] According to the starting compound PEI/N/GQDs,[35] OH, COOH, NH_2, NH, and Ar-H absorptions shifted to a higher frequency in GdNPs/PEI N-doped nanocomposites. The COO+C=N+C-N absorptions shifted to a lower frequency in GdNPs/PEI@N-GQDs nanocomposites. Interestingly, the frequency of COO+C=N absorption bands observed at 1646 cm^{-1} in PEI@N-GQDs was shifted to a lower frequency of 1633 cm^{-1} in GdNPs/PEI N-doped nanocomposites. These results indicate that Gd(III) is reduced to Gd(0) metal by COOH groups on the surface of PEI/N/GQDs. After the reaction, GdNPs/PEI@N-GQDs nanocomposites are formed and COOH groups are converted into CO_2 groups. In this case, the absorption observed at 1633 cm^{-1} is only attributed to the C=N vibration in the material when the COO groups are removed from the molecule. In the literature, the bands corresponding to the vibration of the cubic phase of Gd-O have been defined as approximately 550 and 440 cm^{-1} for nanocomposites doped with Gd_2O_3.[39] In our study, this region of the spectrum cannot be unequivocally attributed to the Gd-O vibration, as it is similar to PEI@N-GQDs.[35] The OH+NH_2+NH absorptions are shifted to a higher frequency in the FTIR spectrum for the GdNPs/PEI@N-GQDs nanocomposite. This is an indication that with the removal of CO_2 groups from the surface, OH groups are formed on the surface instead of CO_2. Figure 2b presents the UV–Vis spectra of the starting compounds Gd (III) nitrate, PEI@N-GQDs,[35] and GdNPs/PEI@N-GQDs nanocomposites.

The Ultraviolet-Visible (UV–Vis) spectra of the compounds were measured using a PG Instruments T80 UV–Vis spectrometer. To compare the electronic transitions in the materials, the UV–Vis spectra of the $Gd(NO_3)_3.6H_2O$, PEI@N-GQDs, and GdNPs/PEI@N-GQDs nanocomposites were recorded (Figure 2b). Two absorptions are observed in the UV–Vis spectrum of $Gd(NO_3)_3{\cdot}6H_2O$. Strong absorption at 244 nm is attributed to ligand-to-metal charge transfer (LMCT), and weak

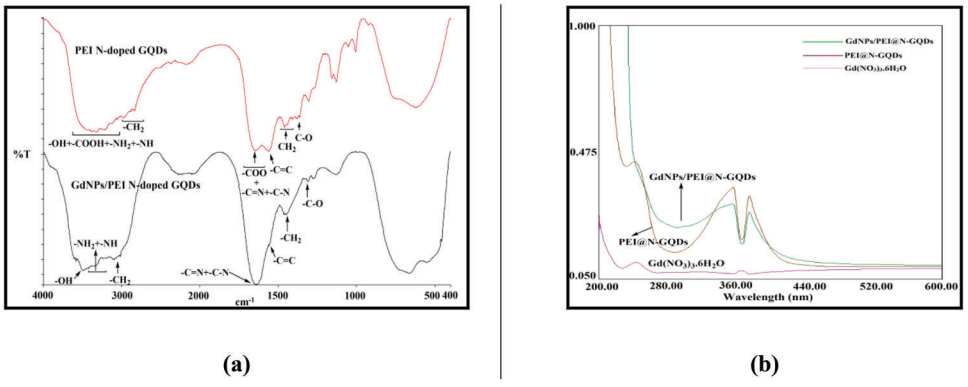

Figure 2. a) FTIR spectra of the starting compounds Gd (III) nitrate the PEI@N-GQDs,[35] and GdNPs/PEI@N-GQDs nanocomposites; b) UV–Vis spectra of the starting compounds Gd(III) nitrate, PEI@N-GQDs, and GdNPs/PEI@N-GQDs nanocomposites.

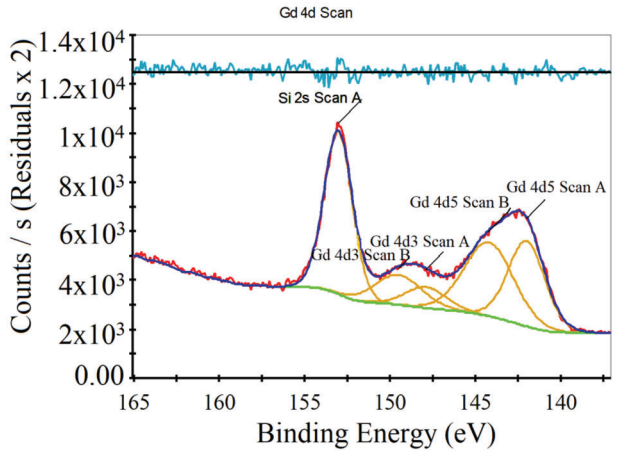

Figure 3. (XPS) spectra of GdNPs/PEI@N-GQDs nanocomposites.

absorption at 364 nm is attributed to f-f transitions. In PEI@N-GQDs, the strong transitions observed at 242 and 367 nm belong to the $\pi \rightarrow \pi^*$ and $n \rightarrow \pi^*$ transitions, respectively. When the UV–Vis spectra of GdNPs/PEI@N-GQDs nanocomposites are examined, a strong shoulder at 247 nm, a weak shoulder at 300 nm, and absorption at 367 nm is observed. The strong shoulder observed at 247 nm and the absorption at 367 nm is attributed to the PEI@N-GQDs in the nanocomposite, and the weak shoulder at 300 nm to the gadolinium nanoparticles. In the UV–Vis spectrum, a weak shoulder was observed at 300 nm in the GdNPs/PEI@N-GQDs nanocomposites, different from the spectrum of the starting materials $Gd(NO_3)_3.6H_2O$ and PEI@N-GQDs, is evidence for the presence of gadolinium nanoparticles. In a study, the optical absorbance spectrum of the Gd_2O_3/CdO composite was investigated, and the absorbance band at 300 nm was attributed to 8S7/2 → 6IJ (f-f) transitions in Gd_2O_3, respectively, and the absorption band at 453 nm was attributed to the transition of CdO crystallites in the nanocomposite.[40] In another study; two absorption peaks at 243 nm (sharp) and 304 nm (broad) were recorded in Gd_2O_3 nanoparticles calcined and shaped at 800 °C. It has been stated that the absorption at 243 nm may occur due to the transition between the valence band and the conduction band, while the weak absorption at 304 nm is due to transitions involving external conditions such as surface traps/defect states/impurities.[41] It has been stated that the smaller-sized particles have a high surface-to-volume ratio, which causes an increase in the defect distribution on the surface of nanomaterials. Nanomaterials with low particle sizes exhibit strong and broad absorption bands. Also, the broad absorption peak at 304 nm, transitions of $^8S_{7/2} \rightarrow {}^6P_{7/2}$, and the sharp absorption peak at 243 nm are given as a feature for all Gd_2O_3 particles attributable to $^8S_{7/2} \rightarrow {}^6I_J$.[41] In our study, the presence of Gd_2O_3 nanoparticles is unlikely, or in trace amounts. As a result, the weak shoulder observed at 300 nm in the UV–Vis spectrum can be attributed to the plasmon peaks of the Gd(0) metal.

XPS was used to characterize the synthesized Gd nanoparticles (**Figure 3**). The binding energy for Gd(4d)3/2 and Gd(4d)5/2 was 149.54 and 144.23 eV, respectively, in the XPS spectrum of the GdNPs/PEI@N-GQDs nanocomposite (Figure 3). For Gd, Gd(III) nitrate pentahydrate and Gd_2O_3, the binding energies of Gd(4d)3/2 are 140.34, 149.00 and 148.10 eV, respectively. For Gd(4d)5/2, the binding energies are 141.7, 143, and 141.8–143.8 eV, respectively.[42] The data for Gd(4d)5/2 and Gd(4d)3/2 are not in good agreement with the data for Gd(III) compounds in the GdNPs/PEI@N-GQDs nanocomposite. In particular, in the GdNPs/PEI@N-GQDs nanocomposite, the Gd(4d)5/2 data are higher. This result makes it more probable and more likely that the Gd is Gd(0) rather than Gd(II). As a result, in the GdNPs/PEI@N-GQDs nanocomposite; It can be said that Gd is Gd(0) from FTIR, UV—Vis, and XPS data.

Other measuring techniques including scanning electron microscope (SEM) with energy dispersive X ray spectroscopy (EDX) detection, also confirmed that additional elements were present. The amounts of elements detected by EDX methods are shown in **Figure 4**a. Carbon, nitrogen, oxygen, and gadolinium are detected on the surface of the samples, as can be seen from the EDX spectrum in Figure 4a. This is where EDX means it only detects elements on the surface. It will never provide complete elemental analysis. However, the EDX data confirms the presence of gadolinium in the sample. The transmission electron microscope (TEM) specimen was prepared to further investigate the material after the sonification of the GdNPs-PEI@N-GQDs solution. A single droplet of the solution was dropped onto the carbon film supported copper grid. After the specimen was dried, the high-resolution TEM (HRTEM) analysis was carried out by the JEOL 2100F 200 kV electron microscope. The structure of the particles was examined using the fast Fourier transform (FFT). The structure and morphology of the GdNPs/PEI@N-GQDs nanocomposite are shown in Figure 4b. The fast Fourier transform of the areas where the lattice fringes were significant shows clear spots at the reciprocal space. These spots were in good agreement with the diffraction from {101} planes of the hexagonal Gd phase with a space group of $P6_3/mmc$ (194). The presence of Gd is also validated by EDS during the TEM analysis. These GdNPs in the PEI@N-GQDs solution have an average particle size of 5 nm.

In the present study, an FS5 spectrofluorometer with an integrating sphere was used to investigate the photoluminescence (PL) performance of GdNPs/PEI@N-GQDs nanocomposites. The samples were diluted (1:10) in DI water. **Figure 5** shows the experimental setup for PL measurement. A 150 W CW Xenon lamp is used as the light source. An excitation monochromator provides an adjustable excitation wavelength. This figure does not show the setup of the all-reflective optics. An adjustable excitation wavelength from 200 to 700 nm can be obtained by using an excitation monochromator. To collect the emitted photons in the wavelength range of 250 to 1000 nm, an emission monochromator is used. The emission spectra of GdNPs/PEI@N-GQDs were recorded for increasing excitation wavelengths in 10 nm steps from 200 to 700 nm. The physics behind this phenomenon can be understood in the following way: When the light source strikes the sample, some electrons are excited to higher energy levels. These electrons then return to their ground energy level and emit radiation. The number of photons emitted as a fraction of the number of photons absorbed is defined as the photoluminescence quantum yield (PLQY) of a molecule or material. At specific wavelengths reflecting the energy difference between the energy levels, this was detected by the PL spectrometer. The PL intensity of the sample can be obtained from $F_I = \Phi \cdot I \cdot B$, where product of $I \cdot B$ is the absorption of light, Φ is the quantum yield

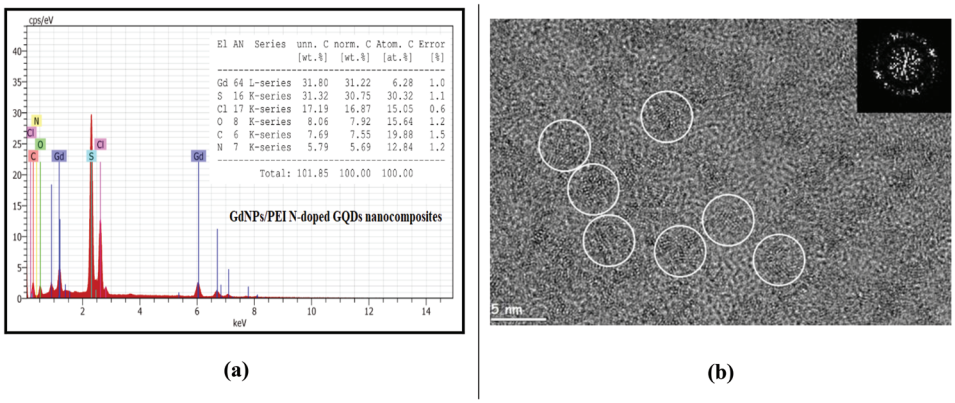

Figure 4. a) EDX analysis of the GdNPs/PEI@N-GQDs nanocomposites; b) HRTEM analysis of GdNPs/PEI@N-GQDs nanocomposites.

of photon excitation. The quantum yield involves both radiative decay and nonradiative decay of excited states as: $\Phi = \Gamma_r/\Gamma_r + \Gamma_{nr}$, where Γ_r is the radiative decay rate and Γ_{nr} is the nonradiative decay rate.[42] The absolute method directly detects all fluorescence in the sample to obtain the quantum yield (QY). PLQY can be calculated by following Equation (1)

$$\text{Quantum yield } (\%) = \frac{S_2}{S_0 - S_1} \times 100 \quad (1)$$

where S_0 is the peak area from incident light, S_1 is the peak area of scattered from the sample, and S_2 is the peak area emitted by the sample. The PLQY and emission spectra of PEI@N-GQDs and GdNPs/PEI@N-GQDs are shown in **Figure 6**a,b, respectively. PEI@N-GQDs and GdNPs/PEI@N-GQDs exhibited maximum PL intensity at 330 and 345 nm, respectively. These correspond to the two peaks in the emission spectrum. This is an indication that the luminescent mechanism for excitation in the UV region is via an interband transition.[42–44] The PL peak is shifted from 330 nm (Gd-free PEI@N-GQDs) to 345 nm by the doping of Gd (GdNPs/PEI@N-GQDs). This is an indication that the luminescence mechanism for excitation in the UV region is via an interband transition.[42–44] The PLQY of GdNPs/PEI@N-GQDs is obtained to be 35.96%. The increase in PLQY is about 470% compared to the Gd-free PEI@N-GQDs sample (7.60%) and the intensity decreases as the excitation wavelength changes, and can be caused by the electronic conjugate structures, emission traps, and surface states of quantum dots.[43–45]

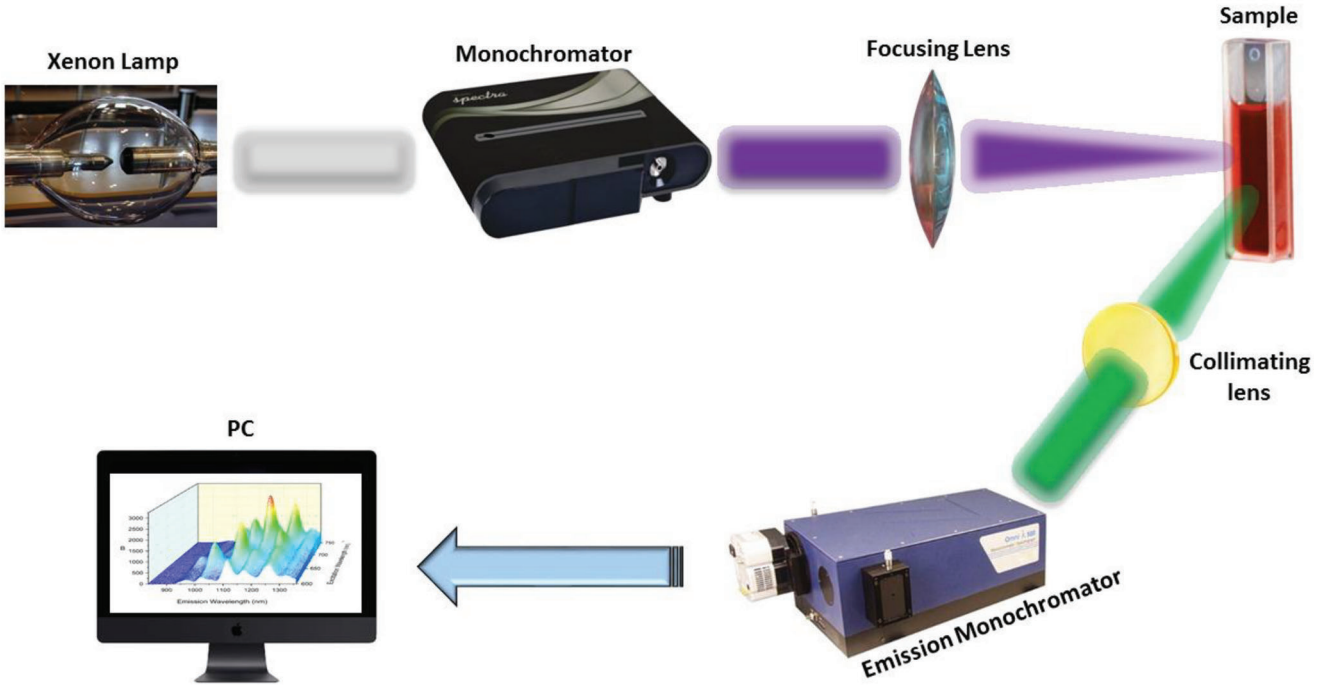

Figure 5. The experimental setup of PL measurement.

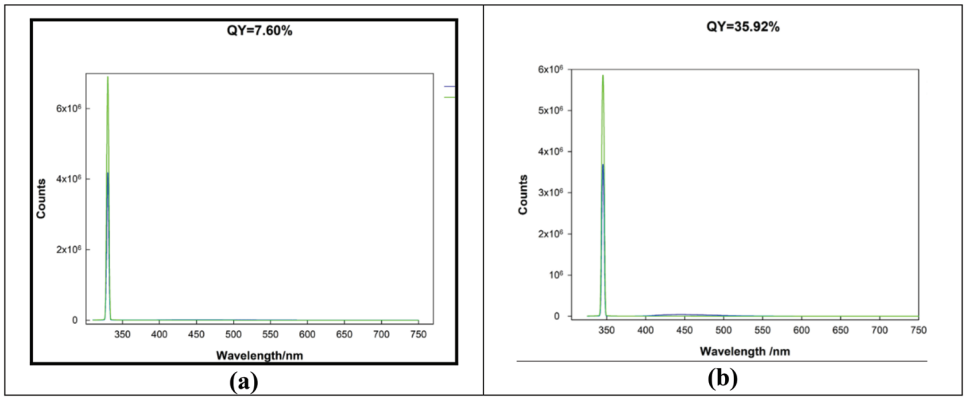

Figure 6. PL spectra of a) PEI@N-GQDs and; b) GdNps/PEI@N-GQDs.

3.2. Electrical Characterization

To determine some electrical properties and parameters of the GdNPs/PEI@N-GQDs nanocomposites interface, forward I–V measurements were performed, confirming the TE theory. The following Equation (2) has been used to construct the diode.[46,47]

$$I = I_0 \left[\exp\left(\frac{q\left(V - IR_s\right)}{nkT} \right) - 1 \right] \tag{2}$$

where I_0, n, V, k, q, IR_s, and T are the reverse saturation current, ideality factor, applied bias voltage, the Boltzmann constant, electronic charge, the voltage drop across, series resistance (R_s), and the temperature (absolute) in Kelvin, respectively. The I_0 value of the nanocomposite diode can be written as in Equation (3),

$$I_0 = AA^* T^2 \exp\left(-\frac{q\phi_B}{kT} \right) \tag{3}$$

where A^* is the value of the Richardson constant value of 32 A cm^{-2} K^{-2} for p Si, and ϕ_B is the effective barrier height. We can also extract the value of ϕ_B value from Equation (3), where A is the Schottky contact area of the structure. The n value is obtained from the slope of the semi-log ln$I$–V plot from Equation (4).

$$n = \frac{q}{kT} \left(\frac{dV}{d\ln I} \right) \tag{4}$$

Figure 7a shows the ln$I$–V plot of the GdNPs/PEI@N-GQDs nanocomposite diode. Two linear regions of this plot are inset in Figure 7, and the n and ϕ_B values obtained over these two regions are 4.9, 16.9, and 0.605, 0.568 eV, respectively. The rectification ratio (RR) was found to be 14 at a voltage of ± 5 V. The structure does not show good rectification, but it can be said that the low RR, which is desired to be high, results from doping with Gd. As is well known from the literature, the TE theory is valid for $V \geq 3kT/q$ which is corresponding to the 0.075 V for 300 K, approximately. As can be seen from the inset in Figure 7a, the forward bias ln$I$-V plot of the GdNPs/PEI@N-GQDs nanocomposite diode has two distinct linear regions with different slopes and intercept points at zero bias voltage. From these regions; the first one (Region 1) corresponds to the 0.075–0.25 V and the second one (Region 2) corresponds to the 0.325–1.075 V.

A Gd-doped GaN Schottky diode for neutron detection has been fabricated in the literature.[23–26] The device fabricated by the researchers[23–26] showed ohmic behavior. This is similar to our results. Due to the presence of the mid-gap defect, the gold-doped, platinum-doped, and niobium-doped devices reported in the literature showed a similar effect. In our previous study,[35] the RR of N-doped PEI functionalized GQDs diode without Gd was found to be 28.10^3 at ± 5 V. In this study, the GdNps doping in the structure is the only distinguishing feature of the diode structure.

In addition to TE theory, employing the approach of the Norde method[48] and the functions of Cheung,[49] ϕ_B, and R_s can be determined. The Cheung method can also be used to calculate n for higher forward biases. Equations (5) and (6) define the current and voltage-dependent functions provided by this method.

$$\frac{dV}{d\ln I} = IR_s + \left(\frac{nkT}{q} \right) \tag{5}$$

$$H(I) = V - \frac{nkT}{q} \ln\left(\frac{I}{AA^* T^2} \right) = IR_s + n\phi_B \tag{6}$$

The dV/dln$I$ and $H(I)$ versus I plots of the GdNPs/PEI@N-GQDs nanocomposite diode are shown in Figure 7b. The R_s values of the structure are the slopes of the plots of these linear functions and were obtained as 2.63 and 2.35 kΩ, respectively. Again, for Equation (5), the n value is extracted from the intercept point of the y-axis of the plot. Since the approximate value of the kT/q at room temperature is 0.026 V, the n value here was found to be 11.6. It can be noted that the n value obtained by this method is the same as the n value obtained at a forward bias (Region 2) in TE theory. Substituting this n value into Equation (6), the ϕ_B is easily obtained; here, it is found to be 0.584 eV.

Norde's approach is also used to obtain ϕ_B and R_s values.[36] For this approach, the relationship in Equation (7) can be given as follows,

$$F\left(V_m\right) = \frac{V_m}{\gamma} - \frac{kT}{q} \left[\ln\left(\frac{IV_m}{AA^* T^2} \right) \right] \tag{7}$$

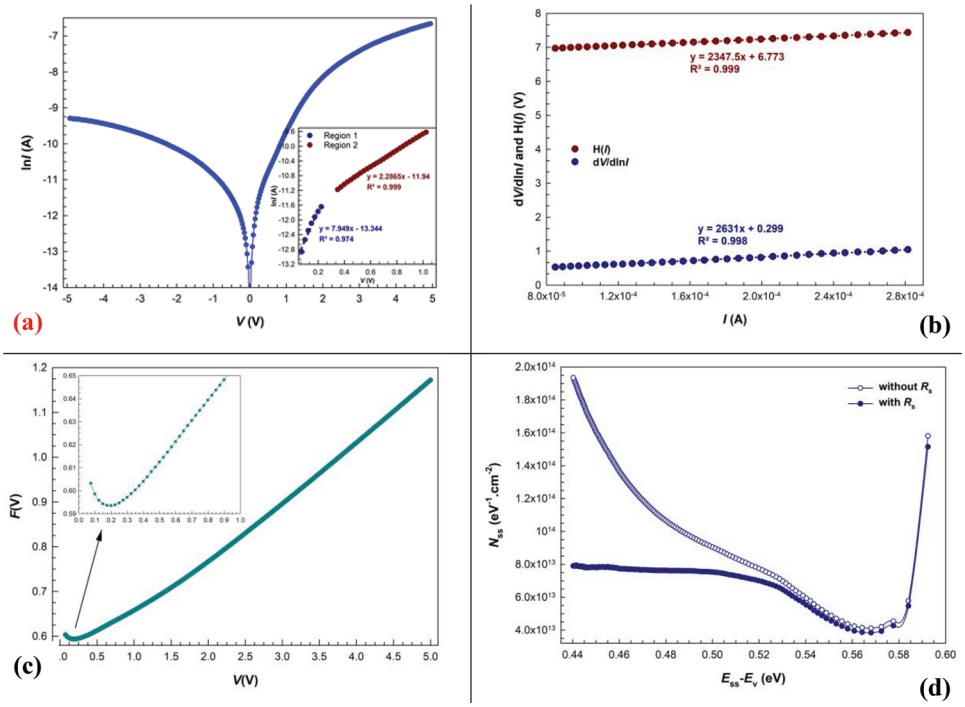

Figure 7. a) The ln*I*–*V* plot with inserted linear regions; b) The d*V*/dln*I* and *H*(*I*) versus *I* plots; c) The *F*(*V*)–*V* plot with inserted minimum values; d) The energy-dependent profile of N_{ss} of the GdNPs/PEI@N-GQDs nanocomposite diode.

where γ is an integer greater than the value of n obtained. ϕ_B is described in the following way (Equation 8)

$$\phi_B = F\left(V_m\right) + \frac{V_m}{\gamma} - \frac{kT}{q} \tag{8}$$

R_s is given in Equation (9),

$$R_s = \left(\frac{kT}{q}\right)\left(\frac{\gamma - n}{I_m}\right) \tag{9}$$

Here $F(V_m)$ is the minimum point of the *F*(*V*)–*V* plot, and I_m is the current corresponding to the minimum voltage value (V_m). Figure 7c shows the *F*(*V*)–*V* plot of the structure, and the V_m and I_m values were defined at the minimum of the *F*(*V*)–*V* curve. By substituting these minimum values in the equations given above, ϕ_B and R_s values are obtained with this approach.

TE theory, together with Norde and Cheung's approaches, was used to characterize the diode parameters of the nanocomposite diode structure. **Table 1** lists the n, ϕ_B, and R_s values obtained from these methods. The ϕ_B values were found to be 0.605 and 0.568 eV for two linear regions (TE theory), 0.584 eV (Cheung method), and 0.595 eV (Norde approach). While the ideality factors of the undoped-Gd structure for the TE theory are 3.71 and 9.20 for the Cheung method in our previous study,[35] the n values are found to be 4.9 and 16.9 for the TE theory and 11.6 for the Cheung method in this study. The use of different regions of the ln*I*–*V* plot explains the different values found for n. The values of R_s are then found to be 3.35 kΩ from the Norde function and 2.63 kΩ and 2.35 kΩ from the Cheung function. The R_s values obtained using Cheung's method are smaller than those obtained using Norde's approach. This can be explained by the fact that Norde's method is performed for the entire forward bias range, whereas Cheung's calculation is performed for a nonlinear high voltage region of the forward bias of the ln*I*–*V* plots. It was observed that the R_s value increased in the structure with Gd (2631 Ω) compared to the structure without Gd doping (143 Ω).[35]

Table 1. The basic diode parameters of GdNPs/PEI@N-GQDs nanocomposite structure..

f [kHz]	V_D [eV]	$N_A \times 10^{16}$ [cm^{-3}]	E_F [eV]	c_2	$\phi_{B(C-V)}$ [eV]	$W_D \times 10^{-5}$ [cm]	$E_m \times 10^4$ [V cm^{-1}]	R_s (5 V) [kΩ]
10	1.068	3.88	0.152	0.559	1.183	1.87	11.1	1.16
30	0.692	2.81	0.161	0.404	0.822	1.76	7.57	0.49
50	0.339	2.10	0.168	0.303	0.648	1.40	4.49	0.40

While the interface composed in Schottky structures is desired to improve the diode characteristics, the surface states/trap levels occurring in the forbidden bandgap of the semiconductor can strikingly affect the electrical measurements. For this reason, it is essential to determine the intensities of these states/levels. In this study, the changes in these states were obtained by four different approaches depending on both voltage and energy. First, the energy-dependent change of N_{ss} was extracted from the voltage-dependent n and ϕ_B using the Card–Rhoderick approach[50] through Equations (10) and (11),

$$n = \frac{q}{kT}\left(\frac{dV}{d\left(\ln I\right)}\right) = 1 + \frac{\delta_i}{\varepsilon_i}\left[\frac{\varepsilon_s}{W_D} + qN_{ss}\right] \tag{10}$$

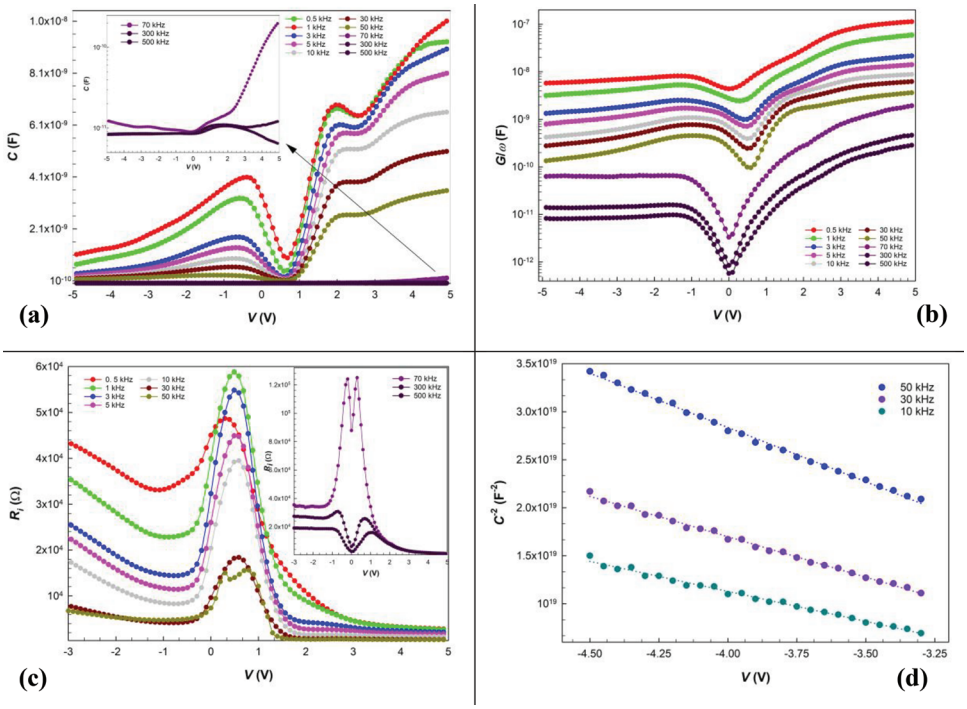

Figure 8. a) The *C*–*V* plots; b) The semi-logarithmic G/ω–*V* plots; c) The R_i–*V* plots with inserted higher frequencies; d) The C^{-2}–*V* plots of the GdNPs/PEI@N-GQDs nanocomposite diode at certain frequencies.

$$\phi_e = \phi_B + \beta\left(V - IR_s\right) = \phi_B + \left(1 - \frac{1}{n\left(V\right)}\right)\left(V - IR_s\right) \tag{11}$$

Furthermore, the energy position of N_{ss} for a p-type semiconductor is given in Equation (12) as follows[50]

$$E_{ss} - E_v = q\left(\phi_e - V\right) \tag{12}$$

The N_{ss} values were obtained and plotted depending on the energy employing the Equations (10–13).

$$N_{ss} = \frac{1}{q}\left[\frac{\varepsilon_i}{\delta}\left(n\left(V\right) - 1\right) - \frac{\varepsilon_s}{W_D}\right] \tag{13}$$

where the width of the depletion layer is represented by W_D and was found by the *C*–*V* measurements. The variations of the N_{ss} with respect to the energy position have been attributed to a specific distribution of their density between the metal and semiconductor bandgap. The effect of R_s is also quite binding in the characteristics of N_{ss}, and this effect is seen in Figure 7d. Considering R_s and hence the voltage drop across it, the N_{ss} intensities decrease significantly.

A series of frequency and voltage-dependent measurements were carried out to investigate the capacitance (C) and conductance (G/ω) characteristics of the structure as well. Thus, the GdNPs/PEI@N-GQDs nanocomposite diode has been studied for a range of frequencies from 0.5 to 500 kHz at ± 5 V. **Figure 8**a,b shows the *C* and semi-logarithmic G/ω versus *V* plots of the structure. Although both graphs show characteristics of a typical MOS structure, significant changes in the *C* and G/ω values were observed between 0.5 kHz and 50 kHz, especially in the weak inversion and accumulation regions. These peak changes corresponding to different bias and frequency values indicate the presence of N_{ss} localized at the interface and the effect of R_s. At 70 kHz and higher frequencies, there were sharp decreases in *C* and G/ω values. Especially in certain voltage ranges, the decrease of these values at different rates compared to each other and the disappearance of the peaks also indicate the striking effect of the N_{ss} in the structure, so much so that this striking effect was also observed in the change of R_s. The variation of R_s as a function of the applied frequency and voltage ranges was plotted in Figure 8c. The peaks that occurred in the range of approximately −0.3 to 1.0 V between 0.5 and 50 kHz gradually decreased as the frequency increased. However, after 70 kHz, while the *C* values were almost anchored in the −1.0 and 1.0 V range, there were sharp-cut decreases in the G/ω values. While these changes were parallel to each other at frequencies of 50 kHz and earlier, this disproportionate change in C and G/ω at higher frequencies resulted in higher value double peaks in R_s. These "untypical" behaviors can be interpreted as the realignment of the N_{ss} localized in this region under the electric field[51] or the effect of Gd on conductivity at these frequencies. Equation (14) below has been used for the determination of R_i.[52]

$$R_i = \frac{G_m}{G_m^2 + \left(\omega C_m\right)^2} \tag{14}$$

R_i is the resistance corresponding to each voltage value, and C_m and G_m are the capacitance and conductance values in the accumulation regions. Hereby, the intrinsic value of R_s, i.e., the value of R_i at high frequency and in the accumulation region, obtained from the equation, was calculated to be approximately

1.07 kΩ at 5 V and 500 kHz. In this part, the basic electrical parameters of the structure were studied employing the Mott–Schottky theory. For this purpose, the C^{-2} versus V linear regions were plotted in Figure 8d for certain frequencies. Using the following Equations (15 and 16), the relevant parameters were obtained from the slope of these plots and the intersection of the V-axis.

$$C^{-2} = \frac{2}{q\varepsilon_s\varepsilon_0 A^2 N_A}\left(V_D - \frac{kT}{q} + V_R\right) \tag{15}$$

$$\phi_{B(C-V)} = c_2 V_0 + \frac{kT}{q} + E_F - \Delta\phi_B \tag{16a}$$

$$N_A = \frac{2}{q\varepsilon_s\varepsilon_0 A^2 \tan\theta} \tag{16b}$$

$$W_d = \sqrt{\frac{2\varepsilon_s\varepsilon_0 V_D}{qN_A}} \tag{16c}$$

$$E_F = \frac{kT}{q}\ln\left(\frac{N_C}{N_A}\right) \tag{16d}$$

where N_A is the concentration of doping atoms, V_D is the diffusion potential ($=V_0 + kT/q$), V_R is the reverse bias voltage, c_2 is the $N_{A(exp.)}/N_{A(theor.)}$, and also known as $1/n$, $\Delta\phi_B$ is the image force barrier lowering, W_d is the depletion layer width, E_F is the Fermi energy level, and E_m is the electric field across the depletion region. All of these parameters, as well as the frequency-dependent Schottky barrier change ($\phi_{B(C-V)}$), are listed in **Table 2**. The decrease of the barrier ($\phi_{B(C-V)}$) from 1.183 to 0.648 eV with increasing frequency indicates the effect of N_{ss} localized in this region on this change. The surface states, which are intensified diversely in different bias regions, can keep up with the ac signal variation at low frequencies and, in this case, can cause significant effects on the C and G measurements. However, values below 10 kHz due to deviations caused by low-frequency noise and values above 50 kHz are not included in Table 2 since C values hardly change at high frequencies.

The variation of the surface states depending on frequency and voltage in impedance measurements and their effects on the measurements are full of surprises. Various surface states and/or trap levels corresponding to each frequency and voltage value may be localized in the bandgap in the junction region. These surface states or traps are usually divided into five groups

Table 2. Some basic electrical parameters of the structure..

Device parameters	TE		Cheung's Method		Norde's Method (for $n = 4.9$)
	Region 1	Region 2	$dV/d\ln I$	$H(I)$	
n	4.9	16.9	11.6	–	–
I_0 [A]	1.6×10^{-6}	6.52×10^{-6}	–	–	7.71×10^{-6}
Φ_B [eV]	0.605	0.568	0.584	–	0.595
R_s [kΩ]	3.85	3.85	2.63	2.35	3.35

in the literature: (i) interface trapped electronic-charges at interlayer/semiconductor interface, (ii) fixed oxide charges located at the junction; (iii) created some oxide trapped charges by radiation, (iv) mobile ionic-charges, and (v) shallow-states located near the conduction or acceptor band (donor/acceptor type).[46–49] The variations of N_{ss} are highly dependent on the calculation method used, which may correspond to different biases applied and the nature of the method. The interface/surface states in these different species and the different polarization mechanisms significantly affect the impedance measurements depending on the applied frequency. Dipole and interfacial polarization, which are especially effective at low frequencies (0.5 to 50 kHz range in our study), cause considerable increases in C and G/ω values. The ability of N_{ss} and dipole polarization directions at low frequencies to keep up with frequency changes, i.e., their lifetime (τ), is the main reason for these increases.

Therefore, the characterization of N_{ss} in such nanostructured devices can be studied with different approaches in the C/G versus V measurements. For example, one of them is the low-high frequency ($C_{lf} - C_{hf}$) method,[53] which requires only one low and one high-frequency measurement and is based on the calculation of the area between these two measurements (plots). For this, the method proposes the following Equation (17).

$$N_{ss} = \frac{C_{ss}}{qA} = \frac{1}{qA}\left[\left(\frac{1}{C_{lf}} - \frac{1}{C_i}\right)^{-1} - \left(\frac{1}{C_{hf}} - \frac{1}{C_i}\right)^{-1}\right] \tag{17}$$

where C_i is the interfacial capacitance obtained at the lowest frequency. Since the effect of N_{ss} on the measurements is more dominant, especially at low frequencies, N_{ss} changes show parallelism with the voltage-dependent change of low frequency (0.5 kHz), as seen in **Figure 9**a. Here, it can be readily said that the surface states are intensified in the reverse and forward bias regions. However, these states can have different intensity values depending on the different ac signal changes applied to the structure, i.e., the frequencies. In general, since they can keep up with low signal changes, decreases in state intensities occur with increasing frequency values. Furthermore, two different methods can be employed to investigate and interpret these frequency-dependent changes in the intensities of N_{ss}. Either of them is the Hill–Coleman (H–C) method, which is used when peaks are seen in the C and G/ω measurements, and the latter is the conductance method (CM), which allows both the N_{ss} changes and their lifetimes (τ) to be compared with the parallel conductance approach. In the H-C method,[54] the G/ω values corresponding to the maximum values of C_m can be substituted into the Equation (18) given below, and the frequency-dependent variation of N_{ss} can be obtained.

$$N_{ss} = \frac{2}{qA}\left(\frac{\left(G_m/\omega\right)_{max}}{\left(\left(G_m/\omega\right)_{max}/C_i\right)^2 + \left(1 - C_m/C_i\right)^2}\right) \tag{18}$$

The variation obtained by this method for the reverse and forward bias regions is plotted in Figure 9b. As can be noticed, the N_{ss} intensities have decreased with increasing frequency in both bias regions. Moreover, the higher N_{ss} values in the forward bias, where the peak values are high, reveal their effect on the measurements. In the range of 0.5 to 50 kHz, where peaks are observed,

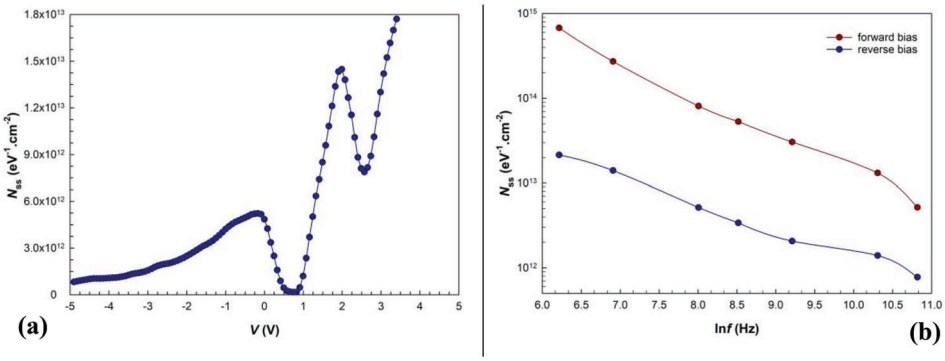

Figure 9. a) The voltage-dependent profile of N_{ss} obtained from the low-high frequencies. b) The N_{ss} versus ln$f$ plots obtained from the H–C method at the reverse and forward biases.

N_{ss} intensities decrease with increasing frequency from 2.14 × 10^{13} to 7.77 × 10^{11} eV^{-1} cm^{-2} for reverse bias and from 6.77 × 10^{14} to 5.18 × 10^{12} eV^{-1} cm^{-2} for forward bias. These higher intensity values obtained in the forward bias can be attributed to the higher increases in C and G/ω values in that region.

In case we want to probe the N_{ss} intensity distributions according to their lifetimes (τ), the most convenient one is the CM.[50] The relationship required for this method, which is based on all frequency measurements and the calculation of the parallel conductance (G_p/ω), is as follows (Equation 19a).

$$\frac{G_p}{\omega} = \frac{\omega G_m C_i}{G_m^2 + \omega^2 (C_i - C_m)^2} = \frac{qAN_{ss}}{2\omega\tau} \ln\left(1 + (\omega\tau)^2\right) \quad (19a)$$

The G_p/ω values are obtained by substituting the C_i value with the C_m and G_m values in the first part of the equation. Then, as seen in **Figure 10**a,b, the G_p versus ln$f$ curves are plotted, and the N_{ss} and τ values are obtained by setting the derivative of the second part of the equation to zero $d\frac{(\frac{G_p}{\omega})_{max}}{d(\omega\tau)}$ at the maximum points of these plots. Thus, the $\omega\tau$ value is found to be 1.98, and with this solution, the simplified form of Equation (19b) is given as follows.

$$N_{ss} = \frac{\left(\frac{G_p}{\omega}\right)_{max}}{0.402qA} \quad (19b)$$

It is seen that there are significant peaks and shifts in these values as a function of frequency in the G_p/ω curves in both reverse and forward bias regions. The variation of N_{ss} and τ values obtained from these peaks are plotted in Figure 10c,d. According to these results, which allow a better interpretation of the rapid changes in the C and G/ω values in both regions, the N_{ss} intensities can show an alteration according to different

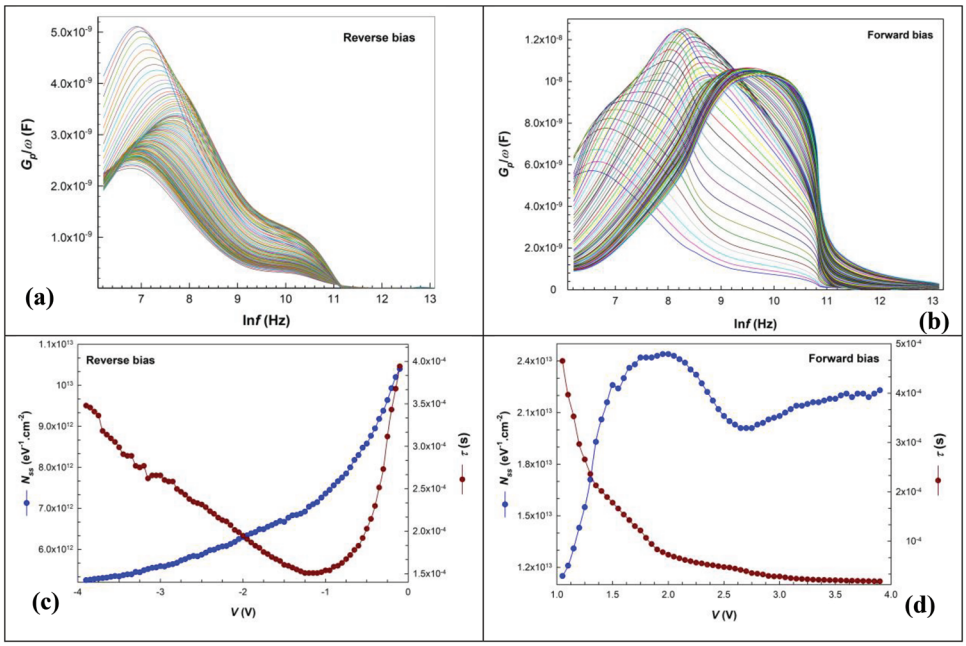

Figure 10. a) The G_p/ω versus ln$f$ plots at the reverse bias. b) The G_p/ω versus ln$f$ plots at the forward bias. c) The voltage-dependent profiles of N_{ss} and τ at the reverse bias. d) The voltage-dependent profiles of N_{ss} and τ at the forward bias of the GdNPs/PEI@N-GQDs nanocomposite diode.

voltage values. The surface states localized in the forbidden bandgap of the semiconductor and the metal, and their residence time distribution at the trap levels, i.e., their lifetimes, can vary depending on both the applied frequency and the voltage. In our previous study,[35] capacitance features, N_{ss}, τ of N-doped PEI-functionalized GQDs diode without Gd were been examined by using the admittance/conductance method. NC behavior was observed in the N-doped PEI-functionalized GQDs diode without Gd at low frequencies. In this study, the GdNps doping in the structure is the only difference in the diode structure. No NC has been observed. This may be attributed to the doping of the rare earth metal Gd into the structure. In this way, we can say that the characterizations performed on such structures are extremely important both to shed light on the physical attitudes of the structures and to ensure their usability as devices in electronic systems. It needs to be investigated how the electrical properties of the structure change when the rare earth elements are doped into carbon-based materials.

4. Conclusion

We present the PL and electrical properties of GdNPs/PEI@N-GQDs nanocomposite-based diode by I–V and $C/(G/\omega)$–V technique at 300 K in the frequency range of 0.5 to 500 kHz at ± 5 V. The absolute PLQY of the GdNPs/PEI@N-GQDs was found to be 35.96%. The increase in quantum yield is approximately 470% compared to the PEI N-doped GQD sample (7.60%) without Gd. This is attributed to the presence of Gd. The ϕ_B values of the diode obtained from TE theory at Region 1, TE theory at Region 2, Norde's, and Cheung's approaches were found to be 0.605, 0.568, 0.584, and 0.595 eV, respectively. However, the RR of the Gd-doped N-doped PEI-functionalized GQDs diode was found to be 14 at a voltage of ± 5 V. Ohmic behavior was observed in the fabricated device. The observed low RR value of the structure may be due to various factors such as barrier height inhomogeneities, surface/interface state or trap levels distributions, doping atom concentrations, and series resistance. The characterizations of N_{ss} have been studied in four different approaches from the I–V and $C/(G/\omega)$–V measurements. The specificity of each method has allowed us to understand the changes in N_{ss} and, thus, their effects, from different viewpoints. Also included are these striking effects on R_s at certain frequencies. The results show how the Gd-doped carbon-based composite interface affects the electrical properties of the structure. Thus, the rapid C and G/ω changes observed as a function of frequency and voltage indicate that such structures are suitable for switching applications. This provided a basis for understanding carbon electronics technology. In this context, it will be necessary to investigate whether other rare earth metals will have similar effects on these structures.

Acknowledgements

The authors are grateful to Gazi University Scientific Research Council (BAP) for the financial support of this research under project number: FGA-2022-8252. The authors would like to thank Prof. Dr. Ahmet Karatay and Dr. Elif Yıldız of Ankara University for providing the EDX spectra.

Conflict of Interest

The authors declare no conflict of interest.

Data Availability Statement

The data that support the findings of this study are available from the corresponding author upon reasonable request.

Keywords

diodes, gadolinium, graphene quantum dots, PEI@N/GQDs, polyethyleneimine functionalized nitrogen-doped graphene quantum dots

Received: April 18, 2023
Revised: June 9, 2023
Published online:

[1] M. J. Molaei, *RSC Adv.* **2019**, *9*, 6460.
[2] X. Guan, Z. Li, X. Geng, Z. Lei, A. Karakoti, T. Wu, P. Kumar, J. Yi, A. Vinu, *Small* **2023**, *19*, e2207181.
[3] M. J. Molaei, *Sci. Rep.* **2022**, *12*, 17681.
[4] D. A. Nguyen, H. M. Oh, N. T. Duong, S. H. Bang, S. J. Yoon, M. S. Jeong, *ACS Appl. Mater. Interfaces* **2018**, *10*, 10322.
[5] E. Haque, J. Kim, V. Malgras, K. R. Reddy, A. Ward, J. You, Y. Bando, S. A. Hossain, Y. R. A. i. Yamauchi, *Small Methods* **2018**, *2*, 1800050.
[6] D. Jiang, Y. Chen, N. Li, W. Li, Z. Wang, J. Zhu, H. Zhang, B. Liu, S. Xu, *PLoS One* **2015**, *10*, e0144906.
[7] L. Liang, X. Peng, F. Sun, Z. Kong, J. W. Shen, *Nanoscale Adv* **2020**, *3*, 904.
[8] S. M. Ghazali, S. A. Izaddin, I. Fatimah, Z. N. Zamil, N. N. Zulkifli, N. Adam, *Open Chem.* **2023**, *21*, 20220285.
[9] P. Tian, L. Tang, K. S. Teng, S. P. Lau, *Mater. Today Chem.* **2018**, *10*, 221.
[10] L. T. Tian, K. S. Teng, S. P. Lau, *Mater. Today Chem.* **2018**, *10*, 221.
[11] S. Zhu, J. Zhang, C. Qiao, S. Tang, Y. Li, W. Yuan, B. Li, L. Tian, F. Liu, R. Hu, H. Gao, H. Wei, H. Zhang, H. Sun, B. Yang, *Chem. Commun.* **2011**, *24*, 6858.
[12] S. Y. Lim, W. Shen, Z. Gao, *Chem. Soc. Rev.* **2015**, *44*, 362.
[13] Q. Tang, W. Zhu, B. He, P. Yang, *ACS Nano* **2017**, *11*, 1540.
[14] P. Dong, B.-P. Jiang, W.-Q. Liang, Y. Huang, Z. Shi, X.-C. Shen, *Inorg. Chem. Front.* **2017**, *4*, 712.
[15] Q. Zhang, J. S. Jie, S. L. Diao, Z. B. Shao, Q. Zhang, L. Wang, W. Deng, W. D. Hu, H. Xia, X. D. Yuan, S. T. Lee, *ACS Nano* **2015**, *9*, 1561.
[16] A. Fatima, M. W. Ahmad, A. K. A. Al Saidi, A. Choudhury, Y. Chang, G. H. Lee, *Nanomaterials* **2021**, *11*, 2449.
[17] A. Rodríguez-Galván, M. Rivera, P. García-López, L. A. Medina, V. A. Basiuk, *J. Cell. Mol. Med.* **2020**, *24*, 3779.
[18] A. Salehabadi, *Elsevier Series on Advanced Ceramic Materials, Advanced Rare Earth-Based Ceramic Nanomaterials* (Ed: S. Zinatloo-Ajabshir), Elsevier, Amsterdam **2022**, pp. 175–203.
[19] J. M. Coey, V. Skumryev, K. Gallagher, *Nature* **1999**, *401*, 35.
[20] B. H. Lee, M. H. Tanvir, D. Lichthardt, R. Gonzalez-Rodriguez, A. V. Naumov, *Nanotechnology* **2020**, *32*, 095103.
[21] D. Abdushukurov, *Gadolinium Foils as Converters of Thermal Neutrons in Detectors of Nuclear Radiation*, Nova Science Publishers, Inc., New York **2011**.
[22] S. L. Ho, H. Yue, T. Tegafaw, M. Y. Ahmad, S. Liu, S.-W. Nam, Y. Chang, H. Lee, *ACS Omega* **2022**, *7*, 2533.
[23] J. Wang, P. Kandlakunta, T. Kent, J. Carlin, D. Hoy, R. Myers, L. Cao, *Trans. Am. Nucl. Soc.* **2011**, *104*, 209.

[24] B. K. Jones, M. McPherson, *Semicond. Sci. Technol.* **1999**, *14*, 667.
[25] B. K. Jones, J. Santana, M. McPherson, *Nucl. Instrum. Methods Phys. Res., Sect. A* **1997**, *395*, 81.
[26] M. J. Molaei, *Sci. Rep.* **2022**, *12*, 17681.
[27] H. Ding, D. Wang, A. Sadat, Z. Li, X. Hu, M. Xu, P. C. de Morais, B. Ge, S. Sun, J. Ge, Y. Chen, Y. Qian, C. Shen, X. Shi, X. Huang, R.-Q. Zhang, H. Bi, *ACS Appl. Bio Mater.* **2021**, *4*, 4798.
[28] B. Ortega-Berlanga, L. Betancourt-Mendiola, C. del Angel-Olarte, L. Hernández-Adame, S. Rosales-Mendoza, G. Palestino, *Crystals* **2021**, *11*, 1094.
[29] M. A. Mashkovtsev, A. S. Kosykh, D. K. Aleshin, E. V. Gordeev, Y. A. Kuznetsova, V. N. Rychkov, A. F. Zatsepin, *Ceram. Int.* **2021**, *47*, 2725.
[30] D. A. Zatsepina, D. W. Boukhvalovc, A. F. Zatsepin, Y. A. Kuznetsova, M. A. Mashkovtsev, V. N. Rychkov, V. Y. Shur, A. A. Esin, E. Z. Kurmaev, *Appl. Surf. Sci.* **2018**, *436*, 697.
[31] A. Karatay, D. Erdener, C. Gürcan, E. A. Yildiz, A. Yilmazer, B. Boyacıoglu, H. Unver, M. Yıldız, A. Elmali, *J. Photochem. Photobiol., A* **2022**, *426*, 113741.
[32] H. El Hamzaoui, G. Bouwmans, B. Capoen, A. Cassez, R. Habert, Y. Ouerdane, S. Girard, D. Di Francesca, N. Kerboub, A. Morana, D. Söderström, A. Boukenter, M. Bouazaoui, *OSA Continuum* **2019**, *2*, 715.
[33] C. Hoehr, A. Morana, O. Duhamel, B. Capoen, M. Trinczek, P. Paillet, C. Duzenli, M. Bouazaoui, G. Bouwmans, A. Cassez, Y. Ouerdane, A. Boukenter, H. El Hamzaoui, S. Girard, *Sci. Rep.* **2019**, *9*, 16376.
[34] D. Söderström, H. Kettunen, A. Morana, A. Javanainen, Y. Ouerdane, H. El Hamzaoui, B. Capoen, G. Bouwmans, M. Bouazaoui, S. Girard, *Sensors* **2021**, *21*, 7523.
[35] Z. B. M. Yıldız, E. Seven, *FlatChem* **2022**, *36*, 100436.
[36] Z. Berktaş, E. Orhan, M. Ulusoy, M. Yildiz, S. Altındal, *ACS Appl. Electron. Mater.* **2023**, *5*, 1804.
[37] E. Efil, N. Kaymak, E. Seven, E. O. Orhan, O. Bayram, S. B. Ocak, A. Tataroglu, *Vacuum* **2020**, *181*, 109654.
[38] N. Kaymak, O. Bayram, A. Tataroğlu, S. Bilge Ocak, E. Oz Orhan, *J. Mater. Sci.* **2020**, *31*, 9719.
[39] M. Ahren, L. Selega, F. Söderlind, M. Linares, J. Kauczor, P. Norman, P.-O. Ka, K. Uvdal, *J. Nanopart. Res.* **2012**, *14*, 1006.
[40] R. Sivasamy, P. Venugopal, E. Mosquera, *Vacuum* **2020**, *175*, 109255.
[41] N. Dhananjaya, H. Nagabhushana, B. M. Nagabhushana, B. Rudraswamy, S. C. Sharma, D. V. Sunitha, C. Shivakumara, R. P. S. Chakradhar, *Spectrochim. Acta, Part A* **2012**, *96*, 532.
[42] A. V. Naumkin, A. Kraut-Vass, S. W. Gaarenstroom, C. J. Powell, *NIST X-ray Photoelectron Spectroscopy Database, NIST Standard Reference Database 20, Version 4.1*, NIST, Gaithersburg, MD, USA **2012**, https://doi.org/10.18434/T4T88K.
[43] Li Changzheng, Y. Yanan, *Nanotechnology* **2014**, *25*, 435703.
[44] S. Zhu, J. Zhang, C. Qiao, S. Tang, Y. Li, W. Yuan, B. Li, L. Tian, F. Liu, R. Hu, H. Gao, H. Wei, H. Zhang, H. Sun, B. Yang, *Chem. Commun.* **2011**, *47*, 6858.
[45] L. Tang, R. Ji, X. Cao, J. Lin, H. Jiang, X. Li, K. S. Teng, C. M. Luk, S. Zeng, J. Hao, *ACS Nano* **2012**, *6*, 5102.
[46] E. E. Tanrıkulu, S. Demirezen, U. I. Altındal, *J. Mater. Sci.* **2018**, *29*, 2890.
[47] R. Joly, S. Girod, N. Adjeroud, P. Grysan, *Sensors* **2021**, *21*, 2253
[48] H. Norde, *J. Appl. Phys.* **1979**, *50*, 5052 .
[49] S. K. Cheung, N. W. Cheung, *Appl. Phys. Lett.* **1986**, *49*, 85.
[50] H. C. Card, E. H. Rhoderick, *J. Phys. D: Appl. Phys.* **1971**, *4*, 1589.
[51] S. M. Sze, K. K. Ng, *Physics of Semiconductor Devices* 3rd ed., John Wiley and Sons, Hoboken **2006**.
[52] E. H. Nicollian, J. R. Brews, *MOS Physics and Technology*, Wiley, New York **1982**.
[53] R. Castagne, A. Vapaille, *Electron. Lett.* **1970**, *6*, 691.
[54] W. A. C. Hill, C. C. Coleman, *Solid State Electronics* **1980**, *23*, 987.